Journal of Nuclear Materials 392 (2009) 63–69

Contents lists available at ScienceDirect

Journal of Nuclear Materials

journal homepage: www.elsevier.com/locate/jnucmat

Circumferential creep properties of stress-relieved Zircaloy-4 and Zr–Nb–Sn–Fe cladding tubes

S.Y. Lee [a,1], K.T. Kim [b], S.I. Hong [a,*]

[a] Department of Nano-materials Engineering, Chungnam National University, Yusung, Daejon 305-764, Republic of Korea
[b] College of Energy and Environment, Dongguk University (Kyungju Campus), Kyungsangbukdo 780-714, Republic of Korea

ARTICLE INFO

Article history:
Received 24 July 2008
Accepted 13 March 2009

ABSTRACT

In this study, the circumferential creep behaviors of stress-relieved Zircaloy-4 and Zr–Nb–Sn–Fe alloys were investigated. The out-of reactor creep resistance of Zircaloy-4 was found to be better than that of the Zr–Nb–Sn–Fe alloy in the temperature and stress range of this study, suggesting that the solution strengthening effect of Sn is more effective in restraining dislocation motion than the precipitate strengthening effect of Nb. Zircaloy-4 and Zr–Nb–Sn–Fe have stress exponents between 6.5 and 7.5 in the lower stress region. The stress exponent decreased to about 3 for Zircaloy-4 and to about 4.2 for Zr–Nb–Sn–Fe in the high stress region. The activation energy increased from 240 to 270 kJ/mol for Zircaloy-4 and Zr–Nb–Sn–Fe as the applied stress increased from 80 to 150 MPa. The creep activation energy observed in this study is close to those of creep for Zircaloy-2 and Zr. The lower stress exponent in the higher stress region for Zircaloy-4 with a relatively higher Sn content compared to Zr–Nb–Sn–Fe alloy may be supported by the fact that the drag force of Sn atoms acting on dislocations increases with increase of Sn content. Larson–Miller Parameter (LMP) decreased with the increase of applied stress, and Zircaloy-4 has a higher LMP than the Zr–Nb–Sn–Fe alloy, compatible with the lower creep rate in Zircaloy-4.

1. Introduction

Zr alloys are being used as fuel cladding tubes and structural materials in nuclear power reactors since they have good high temperature creep resistance and corrosion resistance, good mechanical properties, and low neutron absorption [1]. Zr alloy cladding tubes play important roles not only as the first barrier preventing nuclear fission products in the UO_2 pellet from being released into the reactor coolant, but also as the conductor transferring nuclear fission-induced heat effectively to the coolant. From the viewpoint of the nuclear fuel integrity and the reactor safety, high temperature creep behavior of Zr cladding tubes along with corrosion behavior is one of the key performance parameters to be evaluated since they need to sustain the load arising from the pellet–clad mechanical interaction as well as the load caused by the reactor coolant overpressure acting on the outer surface of the Zr cladding tubes.

The first generation of zirconium alloys includes Zircaloy-4 containing main alloy compositions of Sn, Fe and Cr, which were used for several decades without any significant performance problems. Nuclear power utilities, however, have been pursuing the enhancement of safety and economy of nuclear power plants, which has made the world leading nuclear fuel vendors such as Westinghouse, Areva, MHI (Mitsubishi Heavy Industries), and NFI (Nuclear Fuel Industry) develop the second generation Zr alloys such as Zirlo™ (trademark of Westinghouse Electric Co.), M5™ (trademark of AREVA NP), MDA and NDA, respectively, since 1980. Zirlo™ and M5™ tubes are being commercially used in the world. It is noteworthy that the key alloy elements of the second generation Zr alloys are Nb and Sn. Korea Atomic Energy Research Institute (KAERI) also started to develop the second generation Zr alloy, HANA, from the middle of 1990s. After a successful development of HANA alloy, KAERI has been performing HANA in-reactor verification tests in a research reactor and in one of nuclear power plants in Korea.

Creep characteristics of the second generation Zr alloys have usually been investigated mainly using non-standardized flat specimens from sheets rather than actual cladding tubes because of experimental difficulties. In general, sheets have quite different microstructure including texture and grain structure due to different heat treatment and fabrication processes when compared with Zr alloy cladding tubes. In this study, circumferential creep behaviors of cladding tubes using ring specimens were studied to evaluate the difference of creep behaviors between Zircaloy-4 and a Zr–Nb–Sn–Fe alloy. Creep deformation mechanisms of Zircaloy-4 and a Zr–Nb–Sn–Fe cladding tubes were also examined based on the creep behaviors along with the microstructural analyses. The

* Corresponding author. Tel.: +82 42 821 6595; fax: +82 42 822 5850.
E-mail address: sihong@cnu.ac.kr (S.I. Hong).
[1] Present address: Iljin Duiamond, Eumsung, Chungbuk 369-820, Republic of Korea.

0022-3115/$ - see front matter © 2009 Elsevier B.V. All rights reserved.
doi:10.1016/j.jnucmat.2009.03.045

creep data for the first and second generation Zr alloys in this study may be utilized as a feedback for the design and development of next generation Zr alloys.

2. Experimental method

In this study, stress-relieved cladding tubes of Zircaloy-4 (Zr–Sn–Fe–Cr) (first generation) and Zr–Nb–Sn–Fe alloy (second generation) were selected for studies of mechanical behaviors and creep characteristics. Both alloys were manufactured by cold pilgering with two intermediate heat treatments and the final stress relieving heat treatment at 460 °C for 7 h. Chemical compositions of the two Zr alloys are given in Table 1.

It is well known that the load acting on the cladding tube occurs mainly in the circumferential direction because thermal expansion and swelling of UO_2 pellets tend to load the cladding tube circumferentially. In order to examine the tensile mechanical strengths and creep characteristics in the circumferential direction, the Zr alloy tubes were cut vertically against its axial direction and then ring specimens of 4 mm width were made. In this study, a special grip with two half-cylinders with 1 mm wide space between them was used to strain the ring specimen with maintaining a circular configuration of the ring in contact with the grips all the way during the tests [2–4]. The radius of the half-cylinders was 4.35 mm, which is a half of the inner diameter of the cladding tubes.

Hong et al. [2] reported that axial and circumferential mechanical behaviors of Zr alloys are similar based on tensile strength tests. It was experimentally confirmed that the deformation occurred in the left and right-hand sides of the ring within 5 mm width centered on the split line of two half-cylinders and the optimum gage length was assumed to be 5 mm [2–4]. The load is applied to the ring specimen against the surface of the half cylinder and the force normal to the surface of half cylinder due to the applied load is close to zero in left and right-hand sides of the ring. The force normal to the surface of half cylinder increases rapidly away from these both sides and becomes maximum on the bottom and top parts of the ring, resulting in the drastic increase of the friction force and negligible deformation outside the gage length centered on the split line of two half-cylinders. The strain rate and temperature dependences of strength and ductility of Zircaloy-4 ring specimens assuming the constant gage length were observed to be in reasonably good agreement with those of Zircaloy-4 plate specimens, supporting the assumption of constant gage length [2]. Constant stress creep testers were used to investigate the creep deformation mechanisms of Zr alloys. The tensile testing was performed at room temperature, 450, 480 and 500 °C, while the creep tests were performed at 450, 480 and 500 °C with the applied stress between 80 and 150 MPa. In both creep and tensile testing, pre-heating time was 30 min. Creep rate ($\dot{\varepsilon}$) was measured by LVDT (linear variable differential transformer) with its output voltage amplified through signal conditioner.

The creep-induced fracture surfaces were cleaned in acetone with an ultrasonic cleaner and examined by a scanning electron microscope (SEM). For microstructural analyses of dislocation structure and precipitates, transmission electron microscopy (TEM) specimens were made from the crept rings in the steady-state creep region. With the use of a twin jet polisher immersed in the perchloric acid (10%)–ethanhol solution in the temperature of −40 to −45 °C, 3 mm disks were electro-polished to perforation with the voltage of 12–20 V. TEM specimens were examined by a TEM (JEOL-2010) equipped with an energy dispersive X-ray spectroscopy (EDS) detector with an accelerated voltage of 200 kV.

Table 1
Chemical composition of Zr alloys (wt%).

Element	Nb	Sn	Fe	Cr	O	Zr
Zircaloy-4	–	1.36	0.21	0.11	0.12	Bal.
Zr–Nb–Sn–Fe	1.00	1.00	0.10	–	0.11	Bal.

3. Results and discussion

The ultimate tensile and yield strengths of Zircaloy-4 and Zr–Nb–Sn–Fe alloy at various temperatures are exhibited in Fig. 1. They appear to have typical mechanical characteristics of stress-relieved Zr alloys and the strength decreased rapidly with the increase of temperature. The strengths of Zr–Nb–Sn–Fe alloy appear to be slightly higher than those of Zircaloy-4 although the difference of strengths became larger with increasing temperature. The rapid decrease of mechanical strength up to 450 °C is likely to be caused by the decrease in internal cold work energy resulting from dynamic recovery/recrystallization and the thermally-activated deformation with the increase of temperature. The higher strength of Zr–Nb–Sn–Fe compared to Zircaloy-4 at higher temperature can be linked mostly to the strengthening effect of β-Nb precipitates and in part to solid solution strengthening of Nb atoms at higher temperatures since the major difference of two alloys is the presence of Nb in Zr–Nb–Sn–Fe.

Both Zircaloy-4 and Zr–Nb–Sn–Fe displayed typical creep deformation curves consisting of the primary, secondary and tertiary periods as in Fig. 2. In general, creep rate of Zr alloy claddings is dependent on test temperature, the amount of cold work, and alloying elements. In Fig. 3, the steady-state creep rates of the two Zr alloys at 450, 480 and 500 °C are plotted against the stress. As expected, the steady-state creep rate increases with the increase of temperature and applied stress. It is interesting to note that the steady-state creep rates of the Zircaloy-4 are relatively lower than those of the Zr–Nb–Sn–Fe alloy, in contrast to the higher tensile strength of Zr–Nb–Sn–Fe alloy over Zircaloy-4 (Fig. 1).

In general, Sn atoms exist as substitutional solute atoms in Zr matrix [5,6] and the stress field associated with lattice distortion caused by the difference in atomic radii of Sn and Zr atoms is known to influence the gliding of dislocations and diffusion of vacancies [7]. Sn is also reported to reduce the stacking fault energy of the Zr matrix [8]. The stacking faults are surrounded by partial dislocations, and the stacking fault width is inversely proportional to the stacking fault energy. Dislocation climb and/or cross slip becomes more difficult with the addition of Sn atoms because of a wider spacing between partial dislocations due to low stacking fault energy [9], resulting in the lower creep rates. It can

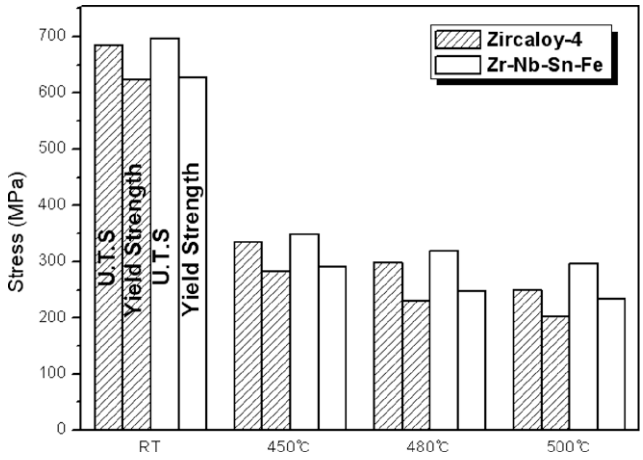

Fig. 1. Yield strengths and ultimate tensile strengths of Zircaloy-4 and Zr–Nb–Sn–Fe.

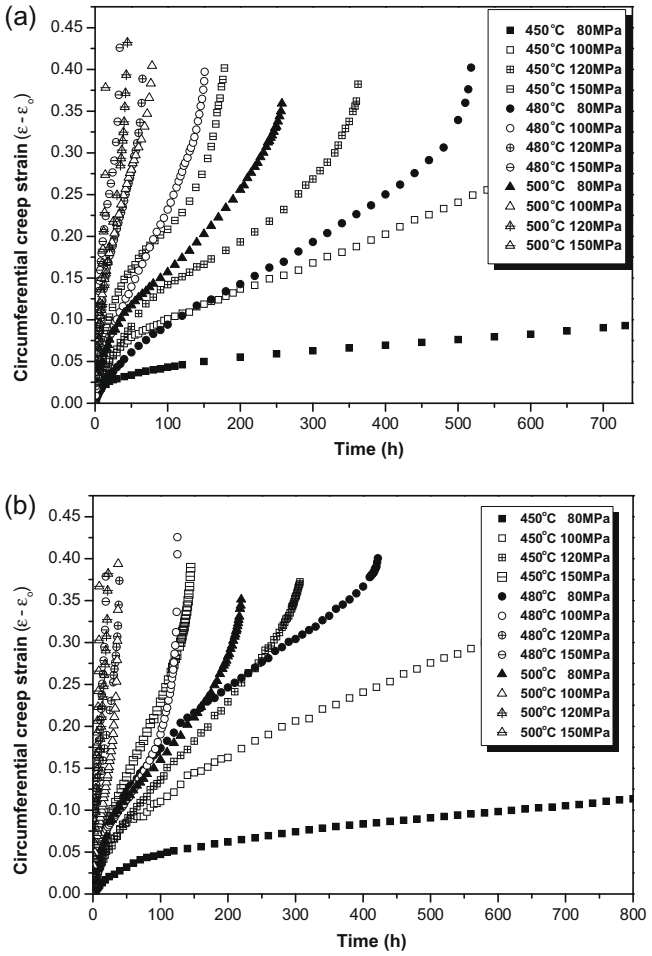

Fig. 2. Creep curves of Zr alloys: (a) Zircaloy-4, (b) Zr–Nb–Sn–Fe.

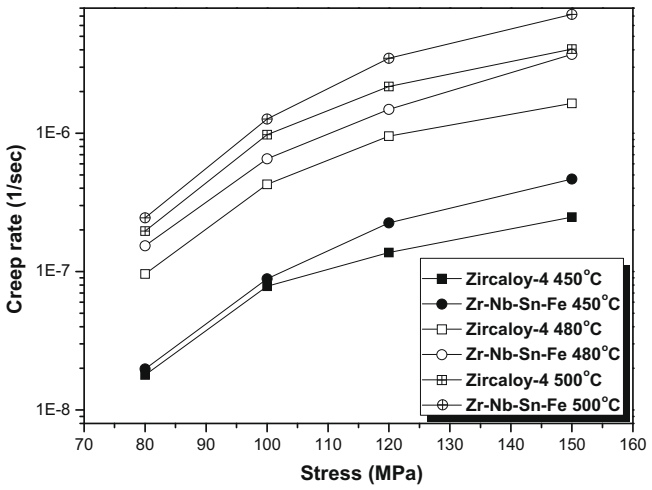

Fig. 3. Effect of stress and temperature on steady-state creep rates of Zircaloy-4 and Zr–Nb–Sn–Fe cladding tubes.

be said that Sn is one of the key alloying elements reducing creep rate in Zircaloy-4 and the steady-state creep rate was found to be lower in Zircaloy-4 with a higher Sn content (1.36 wt%) than Zr–Sn–Fe–Cr alloy with 1.00 wt% Sn.

The maximum solubility of Nb in a Zr–Nb alloy is about 0.2 wt% at 585 °C [10] and, therefore, Nb strengthen the alloy mostly in terms of β-Nb precipitates and/or ZrNbFe type intermetallics. Under the creep conditions of this study [450–500 °C], less than 0.15–0.18 wt% Nb are dissolved in the matrix and strengthen the alloy via solid solution strengthening. The observation that the creep rate of the Zircaloy-4 is lower than that of the Zr–Nb–Sn–Fe alloy suggests that the solution strengthening effect of Sn is more effective in restraining dislocation motion than the precipitate strengthening effects of β-Nb and Nb-containing intermetallics plus the solid solution strengthening of Nb within the solubility limit.

One interesting observation in this study is that the mechanical strength of Zircaloy-4 is lower than Zr–Nb–Sn–Fe alloy, while the creep rate of the former is lower than that of the latter, as shown in Figs. 2 and 3. These seemingly contradictory observations can be explained by the difference of Sn content in two different Zr alloys as explained above. A question still remained to be answered is why Sn in Zircaloy-4 which is supposed to be a key element in lowering the creep rate is not as effective in sustaining the tensile strength at high temperatures. The more effective Sn strengthening in lowering the creep rate can be explained in terms of the dislocation mobility and the diffusivity of Sn. It is noteworthy that the strain rate for the tensile testing is about 1.33×10^{-3}/s, while the creep rate in this study is in the range of 10^{-7}–10^{-8}/s, indicating that the creep strain rate is much lower than the strain rate of tensile testing.

It is now well accepted [9,11,12] that continuous locking of the dislocations along the length is more reasonable than the conventional discrete-obstacle models [13,14] for the solution strengthening model. At high temperatures in which solute atoms is mobile obstacles, dynamic solute-dislocation interaction plays an important role in strengthening [9,15–20]. The solute atoms exert the maximum drag stress in the temperature and strain rate range in which dislocation velocity is similar to the mobility of solute atoms [15–20]. The dislocation velocity in creep testing is quite low so that Sn atoms can segregate at temporarily-stopped dislocations during deformation to exert the appreciable drag stress [11,21]. In tensile testing, however, the contribution of Sn atoms to dynamic solution strengthening is not so effective because the strain rate (i.e., dislocation velocity) is too high. Consequently, it can be said that the addition of Sn can lower the strain rates of Zr alloys appreciably under low strain rate deformation conditions (i.e., creep) although its effect is not as effective at higher strain rates as in tensile testing.

Recently, Charit and Murty studied creep behaviors of recrystallized Nb-modified Zr alloys including Zr–Nb–Sn–Fe and compared them with that of recrystallized Zircaloy-4 [22]. Murty and co-workers [22,23] observed creep rates of recrystallized Zr–Nb–Sn–Fe were lower than those of recrystallized Zircaloy-4 in contrast to the higher creep rate in Zr–Nb–Sn–Fe of the present study. The lower creep rates in Zr–Nb–Sn–Fe compared with Zircaloy-4 observed by Murty and co-workers [22,23] may be attributed to the effect of recrystallization. It is well known that β-phase stabilizers such as Nb and Mo retard the recrystallization and grain growth [24,25]. Therefore, Zr–Nb–Sn–Fe is likely to have a more creep-resistant microstructure than Zircaloy-4 after annealing at high temperatures, resulting in a lower creep rate in Zr–Nb–Sn–Fe. More detailed work on the effect of recrystallization on creep is needed.

In general, creep deformation at intermediate and low temperatures occurs as a result of thermally-activated motion of dislocations. Creep strain rate is usually expressed by the following power-law type relationship [16,18,26]:

$$\acute{\varepsilon} = BD\sigma^n = A\sigma^n \exp(-Q_c/RT), \quad (1)$$

where $\acute{\varepsilon}$ is the steady-state creep rate; σ is the applied stress; A and B are material property-related constants; n is the stress exponent; Q_c is the activation energy for creep deformation; R is the gas con-

stant and T is the absolute temperature. As seen in Eq. (1), the stress exponent, n can be obtained from the slope of the $\ln\dot{\varepsilon}$ vs. $\ln\sigma$ curve at a certain temperature (Fig. 4). As seen in this figure, Zircaloy-4 has stress exponents between 6.5 and 7.5 in the lower stress region and stress exponent of about 3 in the higher stress region. Likewise, Zr–Nb–Sn–Fe alloy has stress exponents between 6.5 and 7.5 in the lower stress region and stress exponent of about 4.2 in the higher stress region.

The activation energy of creep deformation can be derived by Eq. (1) represented by the Arrhenius equation [15,16]. From Eq. (1), activation energy, Q_c can be written as $R[(\partial \ln\dot{\varepsilon})/\partial(1/T)]_\sigma$. Using this relationship, activation energies were calculated in Fig. 5. As seen in this figure, activation energy increases slightly with the increase of stress both in Zircaloy-4 and Zr–Nb–Sn–Fe. This may be explained by the dynamic strain aging effect arising from interaction of dislocations and substitutional Sn atoms [15,16] as will be discussed below.

The power-law creep equation can be modified into the following equation to show the relationship between $\ln(\dot{\varepsilon}/D)$ and $\ln(\sigma/E)$ for the two Zr alloys considered:

$$\dot{\varepsilon}/D = E\Omega/kT(\sigma/E)^n, \tag{2}$$

where Ω is the atomic volume and k is the Boltzmann's constant. Using the Eq. (2), the relationship of $\ln(\dot{\varepsilon}/D)$ and $\ln(\sigma/E)$ for the two Zr alloys are given in Fig. 6. In this figure, a temperature compensated linear relationship between $\ln(\dot{\varepsilon}/D)$ and $\ln(\sigma/E)$ was obtained. The transition of the slope was also observed at a certain value of $\ln(\sigma/E)$.

The transition of the stress exponent from 5–7 to 3–4 have been associated with the transition of the creep deformation mechanism

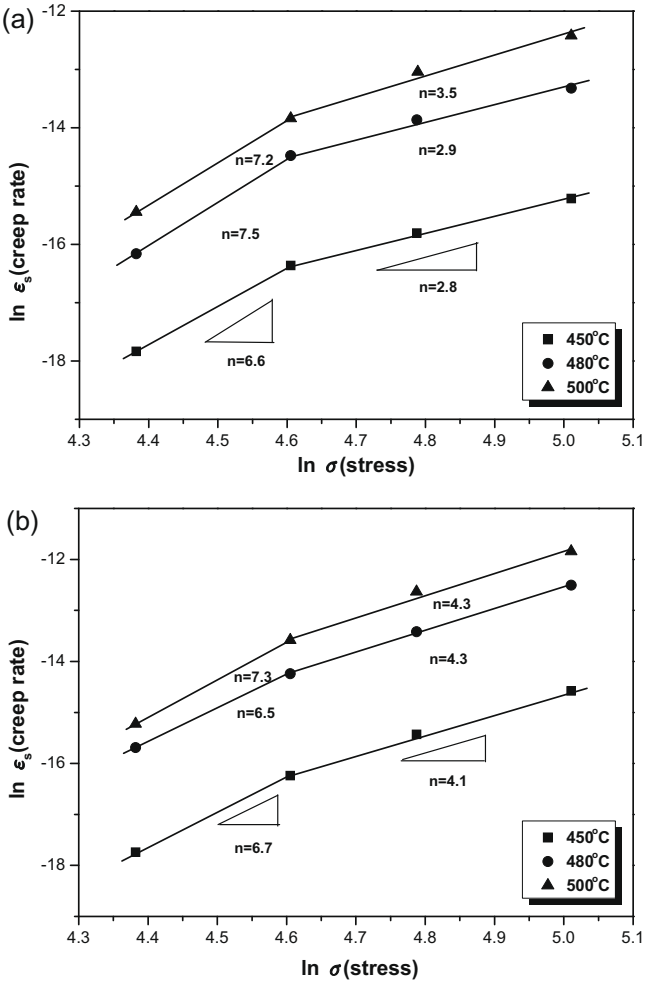

Fig. 4. Relationships between steady-state creep rate and stress for Zr alloys at 450, 480 and 500 °C. (a) Zircaloy-4, (b) Zr–Nb–Sn–Fe.

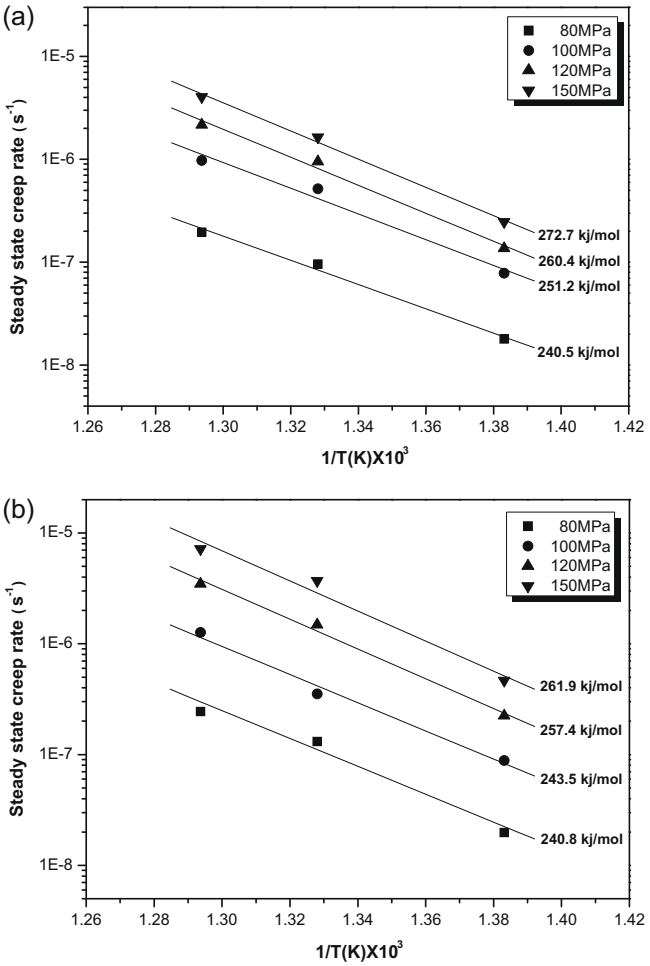

Fig. 5. Steady-state creep rate plotted against $1/T$ for Zr alloys at 450, 480 and 500 °C. (a) Zircaloy-4, (b) Zr–Nb–Sn–Fe.

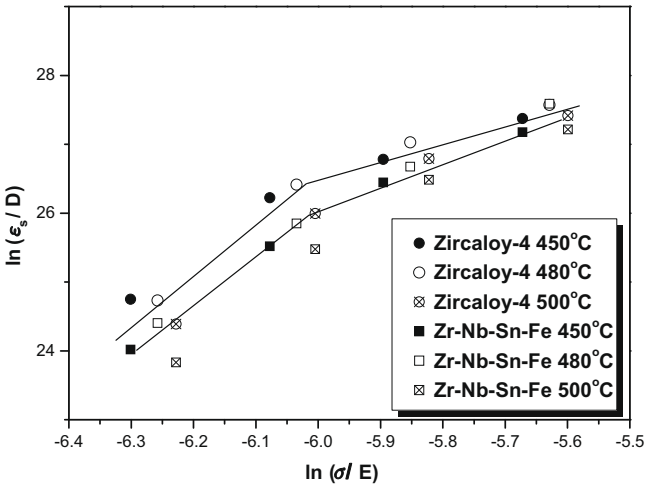

Fig. 6. Temperature compensated creep rate vs. elastic modulus compensated applied stress.

from the climb controlled creep to glide controlled creep [27,28]. Later Hong [15,17,18,29] explained the transition of the stress exponent in terms of the dynamic solute-dislocation interaction. In the dynamic solute-dislocation interaction model, the transition of the stress exponent from 5–7 to 3–4 can be attributed to the increasing solute drag stress due to dynamic solute-dislocation interaction with increase of creep rate (i.e., applied stress). In Zircaloy-4 and Zr–Nb–Sn–Fe, the solute atoms which can be mobile in the temperature range of this study are tin and oxygen atoms. The temperature range in which oxygen atoms exert the maximum drag stress via solute-dislocation interaction under creep condition is much lower than the creep temperature range of this study [16,29–31]. In the temperature and strain rate range for creep of the present study, the mobility of oxygen atoms are too high to exert an appreciable drag stress. Hong [18,29] suggested that the stress exponent in high stress region increases with increasing solute atoms which causes the drag stress. The drag stress of Sn atoms acting on dislocations would also increase with the increase of Sn content, resulting in a little smaller stress exponent in the higher stress range for the Zr–Nb–Sn–Fe alloy with a higher Sn content as observed in Fig. 4. The transition of the stress exponent is clearly observed also in Fig. 6 both for Zircaloy-4 and Zr–Nb–Sn–Fe.

As seen in Fig. 5, activation energy increases slightly with the increase of stress both in Zircaloy-4 and Zr–Nb–Sn–Fe. The activation energy increased from 240 to 270 kJ/mol for Zircaloy-4 as the applied stress increased from 80 to 150 MPa, while it increased from 240 to 260 kJ/mol for Zr–Nb–Sn–Fe alloy. The creep activation energy observed in this study is close to those of creep for Zircaloy-2 (245–287 kJ/mole[32,33]) and Zr (234–271 kJ/mole [33,34]), which is consistent with those of self diffusion in Zr (220–280 kJ/mole [35,36]). One interesting observation here is that the creep activation energy increases with increasing stress as shown in Fig. 5. Yavari et al. [28] reported that the creep activation energy of Al–Mg solid solution alloys increased slightly as the stress increases from the region with the stress exponent n = 4.4 to the region with n = 3.1, which is compatible with the observation of the present study. Hong [15] suggested that the measured creep activation energy is dependent on the drag stress (i.e., solute content) and temperature interval used for the measurement. He showed that the creep activation energy increases with increase of stress for solid solution Al–Mg alloy. He [15–20] suggested that the increase in the activation energy for creep deformation coupled with the decrease in the stress exponent with the increase of applied stress can be explained in terms of the dynamic solute-dislocation interaction. Hong's suggestion was found to agree well with the creep results for the Al–Mg alloys with Mg solution strengthening effect [15–20]. Similarly, the Zircaloy-4 having the relatively higher Sn content than the Zr–Nb–Sn–Fe alloy will have a relatively larger solute-dislocation interaction effect. This drag force causes a relatively lower stress exponent and higher activation energy for Zircaloy-4 in the higher stress region.

Fig. 7 shows the TEM micrographs for the steady-state creep specimens of Zircaloy-4 ((a) and (b)) and Zr–Nb–Sn–Fe ((c) and (d)) tested at 480 °C at the applied stress of 80 MPa. In Fig. 7(a)

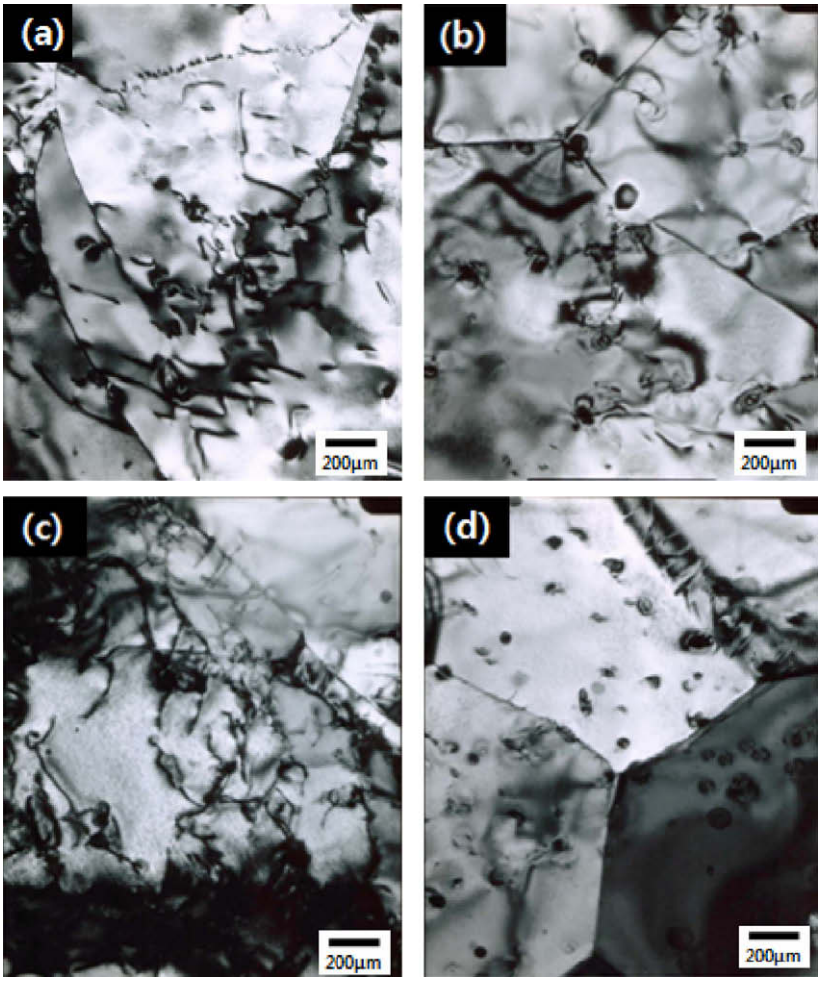

Fig. 7. TEM micrographs of: Zircaloy-4 (a) and (b), and Zr–Nb–Sn–Fe (c) and (d) at 480 °C; (a) and (c) dislocations in contrast, (b) and (d) dislocations out-of contrast to reveal the precipitates more clearly.

and (c), images of dislocations along with particles are shown and only particles are imaged in Fig. 7(b) and (d). It can be seen that recrystallized structures have been well developed in both alloys as a result of coalescence and growth of sub-grains that were developed by generation and rearrangement of dislocations during creep deformation. In addition, the granular-shaped particles are distributed randomly in the matrix, which act as obstacles to dislocation glide. There appears to be no big difference in the size of the precipitates between the two Zr alloys considered. Dislocation tangles were found around the precipitates in Zircaloy-4, as shown in Fig. 7(a), and they appears to consist of geometrically necessary dislocations and some statistically stored dislocations. Similarly, dislocation tangles and pile-ups are observed in the Zr–Nb–Sn–Fe alloy, as shown in Fig. 7(c), and precipitates are distributed randomly in the grains and along the gain boundaries, as shown in Fig. 7(d). In general, the $Zr(Fe,Cr)_2$ precipitates are observed in Zircaloy-4. Based on the EDS analysis, the β-Nb precipitates as well as the precipitates containing Fe alloying element were observed in Zr–Nb–Sn–Fe. This confirms the observation that β-Nb and ZrNbFe precipitates exist in the commercial grade of Zr–Nb–Sn–Fe alloy [37,38].

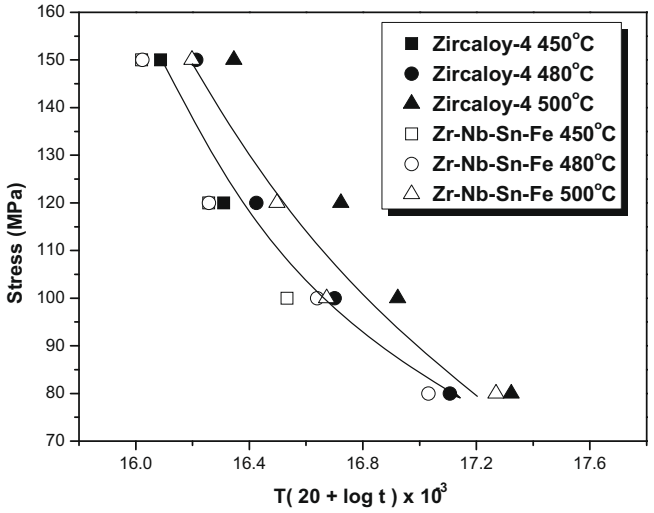

Fig. 8. Larson–Miller plot for Zircaloy-4 and Zr–Nb–Sn–Fe.

The integrity evaluation and life prediction of Zr alloy claddings are needed to maintain the safety of nuclear power plants and to improve its economical efficiency. Creep life decreases sharply with the increase of temperature and stress. Based on the relationship between stress, temperature and creep life, one can predict the creep life at other temperature and stress, if it is known at a certain condition. The prediction methods for the creep life include Larson–Miller Parameter (LMP) [39], Orr–Sherby–Dorn Parameter [40], Manson–Hafred Parameter [41], and Manson–Succop Parameter [42]. In this study, Larson–Miller Parameter (LMP) was selected to evaluate the creep life as follows:

$$\mathrm{LMP} = T\{C + \log(t_r)\}, \tag{3}$$

where T is temperature, C is the material-related constant and t_r is the creep life. The constant C is generally assumed to have a universal value of 20. Fig. 8 shows the relationship between applied stress and LMP. It can be seen that LMP decreases with the increase of applied stress, and Zircaloy-4 (Zr–Sn–Fe–Cr) has a higher LMP than the Zr–Nb–Sn–Fe alloy, compatible with the lower creep rate in Zircaloy-4 (Zr–Sn–Fe–Cr). A negligible dependence of LMP on temperature suggests that C value used in this study (=20) is reasonable. Mayuzumi and Onchi [43] found the creep rupture properties of stress-relieved Zircaloy-4 can be well expressed by the Lason–Miller Parameter. The creep lives of Zircaloy-4 tubes studied by Mayuzumi and Onchi appeared to be slightly higher than those of the present study, which may presumably caused by less stress-relief in their studies (450 °C for 2.5 h compared with 460 °C for 7 h, in the present study).

Fig. 9 shows the SEM images of fractured surfaces of the crept specimens. From this figure, crater-shaped dimples are seen at all temperatures considered. The presence of dimples suggests a typical ductile fracture in general. At 500 °C, some secondary cracks (which propagate perpendicular to the fracture surface) appeared to be formed along the grain boundaries. In general, the fracture mode changes from transgranular to intergranular mode as the temperature increases. With the increase of temperature, the num-

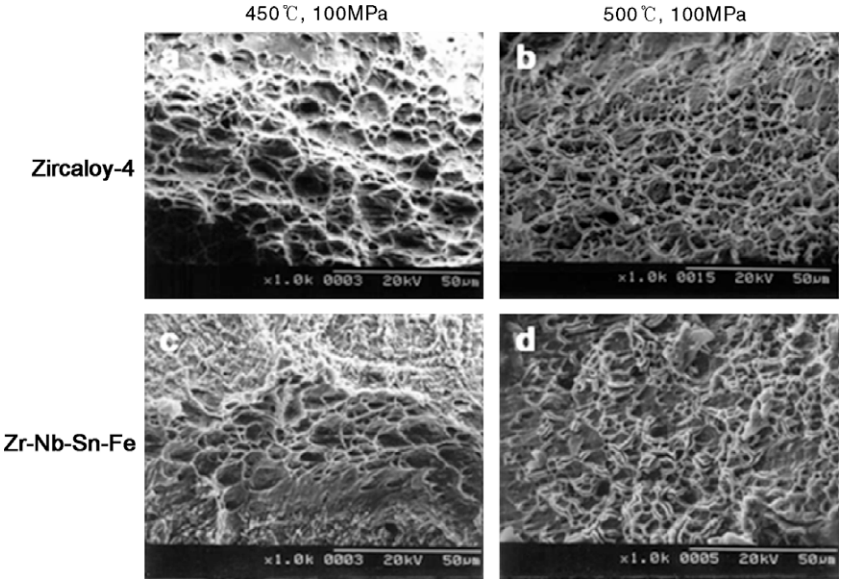

Fig. 9. Creep fracture surfaces of Zircaloy-4 ((a) and (b)) and Zr–Nb–Sn–Fe ((c) and (d)) at 450 °C ((a) and (c)) and 500 °C ((b) and (d)).

ber and mobility of thermal vacancies increase, causing more vacancies or impurities to diffuse to gain boundaries and subsequently fracture mode to change from trans-granular fracture to intergranular one. The comparison of Fig. 9(a) and (b) indicates that the trans-granular fracture mode prevailed at 450, while the secondary cracks along the grain boundaries increased at 500 °C.

4. Conclusions

Creep and tensile tests were performed for Zircaloy-4 and Zr–Nb–Sn–Fe and the results can be summarized as follows:

1. The tensile strengths of Zr–Nb–Sn–Fe alloy were higher than those of Zircaloy-4. The higher strength of Zr–Nb–Sn–Fe compared to Zircaloy-4 at higher temperature can be linked mostly to the strengthening effect of β-Nb precipitates and in part to solid solution strengthening of Nb atoms at higher temperatures since the major difference of two alloys is the presence of Nb in Zr–Nb–Sn–Fe.
2. The out-of reactor creep resistance of Zircaloy-4 was found to be better than that of the Zr–Nb–Sn–Fe alloy in the temperature and stress range of this study, suggesting that the solution strengthening effect of Sn is more effective in restraining dislocation motion than the precipitate strengthening effects of β-Nb and Nb-containing intrmetallics plus the solid solution strengthening of Nb.
3. Zircaloy-4 and Zr–Nb–Sn–Fe have stress exponents between 6.5 and 7.5 in the lower stress region. In the high stress region, the stress exponent decreased to about 3 for Zircaloy-4 and to about 4.2 for Zr–Nb–Sn–Fe. The reduction of stress exponent in the higher stress region can be explained in terms of the dynamic solute-dislocation effect caused by substitutional Sn atoms. The lower stress exponent in the higher stress region for Zircaloy-4 with a relatively higher Sn content compared to Zr–Nb–Sn–Fe alloy may be supported by the fact that the drag force of Sn atoms acting on dislocations increases with increase of Sn content.
4. The activation energy for creep deformation increased from 240 to 270 kJ/mol when the applied stress increase from 80 to 150 MPa for Zircaloy-4, while that of Zr–Nb–Sn–Fe increased from 240 to 260 kJ/mol for the Zr–Nb–Sn–Fe alloy. The creep activation energy observed in this study is close to those of creep for Zircaloy-2 (245–287 kJ/mole) and Zr (234–271 kJ/mole), which is consistent with those of self diffusion in Zr (220–280 kJ/mole).
5. Larson–Miller Parameter (LMP) decreased with the increase of applied stress, and Zircaloy-4 (Zr–Sn–Fe–Cr) has a higher LMP than the Zr–Nb–Sn–Fe alloy, compatible with the lower creep rate in Zircaloy-4 (Zr–Sn–Fe–Cr). A negligible dependence of LMP on temperature suggests that C value used in this study (=20) is reasonable.
6. Creep fracture surfaces exhibited the ductile fracture both in Zircaloy-4 and Zr–Nb–Sn–Fe. The trans-granular fracture mode prevailed at 450 °C, while the secondary cracks along the grain boundaries increased at 500 °C.

Acknowledgement

The authors acknowledge the support from MOCIE (Ministry of Commerce, Industry and Energy), funded through Korea Nuclear Fuel Co. (2007).

References

[1] E. Kohn, ASTM STP 633 (1977) 402.
[2] K.W. Lee, S.K. Kim, K.T. Kim, S.I. Hong, J. Nucl. Mater. 295 (2001) 21.
[3] S.I. Hong, K.W. Lee, K.T. Kim, J. Nucl. Mater. 303 (2002) 169.
[4] S.I. Hong, K.W. Lee, J. Nucl. Mater. 340 (2005) 203.
[5] G.J.C. Carpenter, E.F. Ibrahim, J.F. Watters, J. Nucl. Mater. 102 (1981) 280.
[6] R.J. Perez, C. Toffolon-Masclet, J.M. Joubert, B. Sundman, Calphad 32 (2008) 593.
[7] O.S. Ivanov, U.K. Grigorovitch, in: Second International Conference on Peaceful Uses of Atomic Energy, Genova, vol. 5, 1958, p. 34.
[8] W.A. Mcinteer, David L. Baty, K.O. Stein, ASTM STP 1023 (1989) 621.
[9] S.I. Hong, C. Laird, Acta Metall. Mater. 38 (1990) 1581.
[10] H.G. Kim, J.Y. Park, Y.H. Jeong, J. Nucl. Mater. 347 (2005) 140.
[11] U.F. Kocks, Metall. Trans. 16A (1987) 2109.
[12] Z.S. Basinski, R.A. Foxall, R. Pascual, Scr. Metall. 6 (1972) 807.
[13] R.L. Fleischer, Acta Metall. 11 (1963) 203.
[14] R.L. Fleischer, Acta Metall. 9 (1961) 996.
[15] S.I. Hong, Mater. Sci. Eng. 86 (1987) 211.
[16] S.I. Hong, Mater. Sci. Eng. 64 (1984) L19.
[17] S.I. Hong, Mater. Sci. Eng. 91 (1987) 137.
[18] S.I. Hong, Mater. Sci. Eng. 82 (1986) 175.
[19] S.I. Hong, Mater. Sci. Eng. 79 (1986) 1.
[20] S.I. Hong, Scr. Mater. 40 (1998) 217.
[21] A. Van den Beukel, J. Blonk, G.H. van Haastert, Acta Metal. Mater. 31 (1983) 69.
[22] I. Charit, K.L. Murty, J. Nucl. Mater. 374 (2008) 354.
[23] K.L. Murty, J.R. Wiratmo, Nucl. Eng. Design 156 (1995) 359.
[24] Y.B. Chun, S.K. Hwang, M.H. Kim, S.I. Kwun, Y.S. Kim, J. Nucl. Mater. 265 (1999) 28.
[25] V.D. Hiwarkar, S.K. Sahoo, I. Samajdar, K. Narasimhan, K.V. Mani Krishna, G.K. Dey, D. Srivastava, R. Tewari, S. Banerjee, J. Nucl. Mater. 384 (2009) 30.
[26] E.C. Norman, S.A. Duran, Acta Metall. 18 (1970) 723.
[27] F.A. Mohamed, T.G. Langdon, Acta Metall. 22 (1974) 779.
[28] P. Yavari, F.A. Mohamed, T.G. Langdon, Acta Metall. 29 (1981) 1495.
[29] S.I. Hong, Mater. Sci. Eng. 110 (1989) 125.
[30] S.I. Hong, W.S. Ryu, C.S. Rim, J. Nucl. Mater. 120 (1984) 1.
[31] S.I. Hong, W.S. Ryu, C.S. Rim, J. Nucl. Mater. 116 (1983) 314.
[32] J.J. Holmes, J. Nucl. Mater. 13 (1964) 137.
[33] I.M. Bernstein, Trans. AIME 239 (1967) 1518.
[34] M. Pahutova, J. Cadek, Mater. Sci. Eng. 11 (1973) 151.
[35] M.C. Naik, R.P. Agarwala, Acta Metall. 15 (1967) 1521.
[36] G.M. Hood, R.J. Schultz, Acta Metall. 22 (1974) 459.
[37] C. Toffolon-Masclet, T. Guilbert, J.C. Brachet, J. Nucl. Mater. 372 (2008) 367.
[38] W. Liu, Q. Li, B. Zhou, Q. Yan, M. Yao, J. Nucl. Mater. 341 (2005) 97.
[39] F.R. Larson, J. Miller, Trans. ASME 74 (1952) 74.
[40] R.L. Orr, O.D. Sherby, J.E. Dorn, Trans. ASME 46 (1954) 113.
[41] S.S. Manson, A.M. Hafred, NASA-TN-2890, March 1953.
[42] S.S. Manson, G. Succop, ASTM Spec. Tech. Publ. No. 174 (1956) 40.
[43] M. Mayuzumi, T. Onchi, J. Nucl. Mater. 175 (1990) 135.